nature communications



Article

https://doi.org/10.1038/s41467-024-54647-7

Dynamic fibrillar assembly of αB-crystallin induced by perturbation of the conserved **NT-IXI** motif resolved by cryo-EM

Received: 28 March 2024

Accepted: 18 November 2024

Published online: 28 November 2024

Check for updates

Russell McFarland^{1,2,3,4}, Rozhan Noroozi^{1,2}, Adam P. Miller^{1,2} & Steve L. Reichow 1,2,3

αB-crystallin is an archetypical member of the small heat shock proteins (sHSPs) vital for cellular proteostasis and mitigating protein misfolding diseases. Gaining insights into the principles defining their molecular organization and chaperone function have been hindered by intrinsic dynamic properties and limited high-resolution structural analysis. To disentangle the mechanistic underpinnings of these dynamical properties, we ablate a conserved IXI-motif located within the N-terminal (NT) domain of human αBcrystallin implicated in subunit exchange dynamics and client sequestration. This results in a profound structural transformation, from highly polydispersed caged-like native assemblies into an elongated fibril state amenable to high-resolution cryo-EM analysis. The reversible nature of this variant facilitates interrogation of functional effects due to perturbation of the NT-IXI motif in both the native-like oligomer and fibril states. Together, our investigations unveil several features thought to be key mechanistic attributes to sHSPs and point to a critical significance of the NT-IXI motif in αB-crystallin assembly, polydispersity, and chaperone activity.

Small heat shock proteins (sHSPs) are a conserved family of protein chaperones, critical for maintaining cellular proteostasis¹⁻³. These holdases recognize and sequester destabilized proteins (aka clients), preventing detrimental aggregation events in an ATP-independent manner. The sequestered client remains in a refolding-competent state that may be rescued by ATP-dependent chaperones, like the HSP70 system⁴. Ten sHSP proteins (HSPB1-10) are found in human that are differentially expressed throughout the body^{5,6}. HSPB5 (aka, αB-crystallin; CRYAB) is considered an archetype of the mammalian sHSP family and is ubiquitously expressed, with high levels in the eye lens, cardiac and neuronal tissues^{7,8}. Because of its critical physiological roles, aberrant function or dysregulation of αB-crystallin is associated with a variety of protein misfolding diseases, including cataract, Alzheimer's disease, Parkinson's disease, neuromuscular disease, as well as some cancers9,10.

Despite the physiological significance and involvement in various diseases linked to sHSPs, our grasp of these processes remains constrained by the insufficiency of high-resolution structural insights into this system^{11,12}. This limitation stems from the complex dynamics exhibited by eukaryotic sHSPs that can form high-order assemblies. Under normal conditions, αB -crystallin forms a continuum of large polydispersed oligomers (~10-40 subunits)¹³⁻¹⁶, characterized by rapid subunit exchange¹⁷⁻²⁰. These inherent dynamics are pivotal to the chaperone mechanism, enabling sHSP's to effectively scavenge and sequester a diverse range of client proteins²¹. At the subunit level, αB-crystallin (20.2 kDa) features a tripartite domain organization seen in other sHSPs 22,23 . Central to this is a conserved α -crystallin domain (ACD, ~80 residues in αB-crystallin) shared by all sHSPs. This domain acts as a structural hub, flanked by a variable N-terminal domain (NTD, ~65 residues in αB-crystallin) and C-terminal domain

¹Department of Chemical Physiology and Biochemistry, Oregon Health & Science University, Portland, OR, USA. ²Vollum Institute, Oregon Health & Science University, Portland, OR, USA. ³Department of Chemistry, Portland State University, Portland, OR, USA. ⁴Present address: Analytical and Formulation Sciences, KBI Biopharma, Boulder, CO, USA. e-mail: reichow@ohsu.edu

(CTD, ~28 residues in αB -crystallin) that are both highly dynamic and flexible $^{24-26}$.

The NTD and CTD endow many sHSPs with the capacity to form polydispersed high-order oligomeric structures. Truncated mutants that lack these domains form stable ACD dimers, considered the fundamental building blocks of sHSPs that have been well-characterized structurally $^{27-31}$. Within αB -crystallin and other eukaryotic sHSPs, the CTD performs a well-established role in oligomerization, a process facilitated by a conserved 'IXI-motif' (with X indicating a variable sequence position), followed by an extension of polar and charged residues that enhance overall solubility $^{32-34}$. The influence of the CT-IXI motif on oligomer assembly involves domain-swapping interactions, including binding to a hydrophobic groove located in the ACD.

While the NTD shows considerable sequence variability across sHSPs, it contains regions that remain relatively conserved among eukaryotic sHSPs that exhibit a high degree of hydrophobicity and are similarly involved in multiple interactions with the ACD within the context of native oligomeric formations^{24,35,36}. The functional role of the NTD is less clearly defined but has been acknowledged for its involvement in client binding and specificity, as well as oligomer assembly^{21,37,38}.

Notably, the NTD in αB -crystallin contains an additional IXI-motif located near the beginning of the polypeptide chain (residues 3-5), shown to be involved in client recognition 38 . This N-terminal motif is also present in other sHSPs, such as HSPB3, HSPB4/ αA -crystallin, and HSPB6 (Fig. 1a), where isoleucine is sometimes found as valine. Current models suggest the NT-IXI competes with the CT-IXI motif for binding to the hydrophobic groove at the ACD, contributing to subunit exchange dynamics and oligomer assembly 36 . Due to these various forms of dynamics, structural investigations of full-length αB -crystallin and other high-order sHSPs have so far been constrained to relatively low-resolution or integrative models $^{39-42}$.

In this study, we aimed to explore the impact of disrupting the competition between the CT-IXI and NT-IXI motifs through mutational ablation of the NT motif. Our hypothesis was that silencing the NT-IXI motif might reduce polydispersity, making the system more amenable to high-resolution structural analysis. Remarkably, introducing an NT-AXA variant into human αB crystallin (αB-AXA), where conserved isoleucines were replaced by alanines, led to the emergence of highly elongated and helical fibril assemblies formed during cellular expression. The isolated fibrils are non-amyloid in nature and shared general morphological features to the client-induced elongated states of aBcrystallin we recently described16, but with regular helical features. Cryo-electron microscopy (cryo-EM) resolved the fibril assembly at ~3.4 Å resolution, providing high-resolution structural and mechanistic insights. The fibril state of αB-crystallin displays features, thought to be essential for native sHSP oligomers, including roles of the NTD and CTD in high-order assembly and significant conformational plasticity, and potentially provides key insight into the mechanism of client-induced structural changes. Purified fibrils were fully reversible with native-like caged oligomers upon mild temperature changes (25-42 °C), with fibrils favored at lower temperatures. This allowed for functional dissection of chaperone activity in both the fibril and native-like oligomer states, unveiling varying degrees of impairment in chaperone activity compared to wildtype when tested against the model aggregating client, lysozyme. These findings offer longsought insights into the fundamental principles governing sHSP assembly and dynamics, shedding light on the pivotal role of the conserved NT-IXI motif in α B-crystallin and its dynamic interplay with the CT-IXI, and the profound ability of sHSP's to undergo dramatic morphological rearrangement in response to varying conditions.

Results

Disrupting the conserved NT-IXI motif transforms αB -crystallin into helical fibrils

The NT-IXI motif in αB -crystallin, represented as IAI, is well conserved among model mammalian species (Fig. 1a and Supplemental Fig. 1). To comprehensively assess the structural and functional implications of this duplicate IXI-motif, we engineered a variant of the human αB -crystallin gene, introducing alanine substitutions in place of the conserved isoleucines. This NT-AXA variant (αB -AXA) was expressed in bacterial cells and purified without the use of purification tags or other changes to the gene sequence, using a procedure adapted for wildtype αB -crystallin (αB -wt) (Fig. 1b and Supplemental Fig. 2)^{1,16}. In consideration of the sensitivity of αB -wt oligomerization to environmental conditions, including factors like pH and divalent cations⁴³, the ensuing structural and functional investigations were conducted in consistent buffer conditions containing 20 mM HEPES (pH 7.4), 150 mM NaCl and 1 mM EDTA, in accordance with our previous structural characterizations¹⁶.

Size-exclusion chromatography (SEC) analysis of isolated αB -AXA initially revealed a significant degree of enhanced polydispersity and potential aggregation. The elution profile of αB -AXA exhibited a major peak that coincided with the elution profile of αB -wt (* in Fig. 1b). Additionally, an overlapping broad peak was observed, extending towards the high molecular weight void volume of the SEC column († in Fig. 1b). Further examination by electron microscopy (EM) of negatively stained samples extracted from these primary elution peaks identified two predominant species. The fraction showing elution overlap with αB -wt mainly consisted of spherical oligomers, measuring approximately 14–16 nm in diameter (Fig. 1c, *), consistent with previous characterizations of αB -wt αB -vt (see also Supplemental Fig. 2).

Interestingly, the high-molecular weight fractions exclusively displayed fibrillar structures with distinct helical features (Fig. 1c, †). Employing reference-free two-dimensional (2D) class-averaging techniques, the helical fibril dimensions were determined to have a diameter of about 15 nm and a helical periodicity of around 45 nm. Striated features could be clearly resolved, arranged transversely to the principal helical axis of the fibrils, with an interval of approximately 5 nm. Within the high-molecular weight SEC fractions, fibrils exhibited varying lengths, extending up to -250 nm. Notably, 2D class-averaging analysis applied to the lower-molecular weight fractions uncovered the presence of short fibril assemblies (or protofibrils) in addition to the native-like oligomeric species (comparison of top and bottom 2D classes in Fig. 1c,*).

High-resolution structural analysis of αB -crystallin NT-AXA fibrils by cryo-EM

The distinctive order observed in the α B-AXA fibrils suggested the potential for subjecting them to high-resolution structural analysis by cryo-electron microscopy (cryo-EM). To achieve this, we conducted further biochemical optimization of α B-AXA fibrils, as described in detail below and in the Methods section. The acquired datasets underwent image processing routines utilizing a combination of helical and single-particle methodologies implemented in cryoSPARC⁴⁶, resulting in a final refined density map resolved to a global resolution of ~3.4 Å (Fig. 1d, e; Supplemental Figs. 3 and 4; and Supplemental Table 1)

The dimensions of the resolved fibrils have a diameter of approximately 125 Å, with a refined helical periodicity measuring 480 Å, characterized by a rise of 40.6 Å and twist of 31.7° for the repeating asymmetric unit. The overall quality of the map facilitated the construction of an atomistic model covering the canonical ACD (blue, residues - 75-148) and the majority of the CTD (red and orange, residues 149-161) (Fig. 1f, g; Supplemental Figs. 1 and 4; Supplemental Movie 1). The last 14 residues could not be fully resolved, presumably

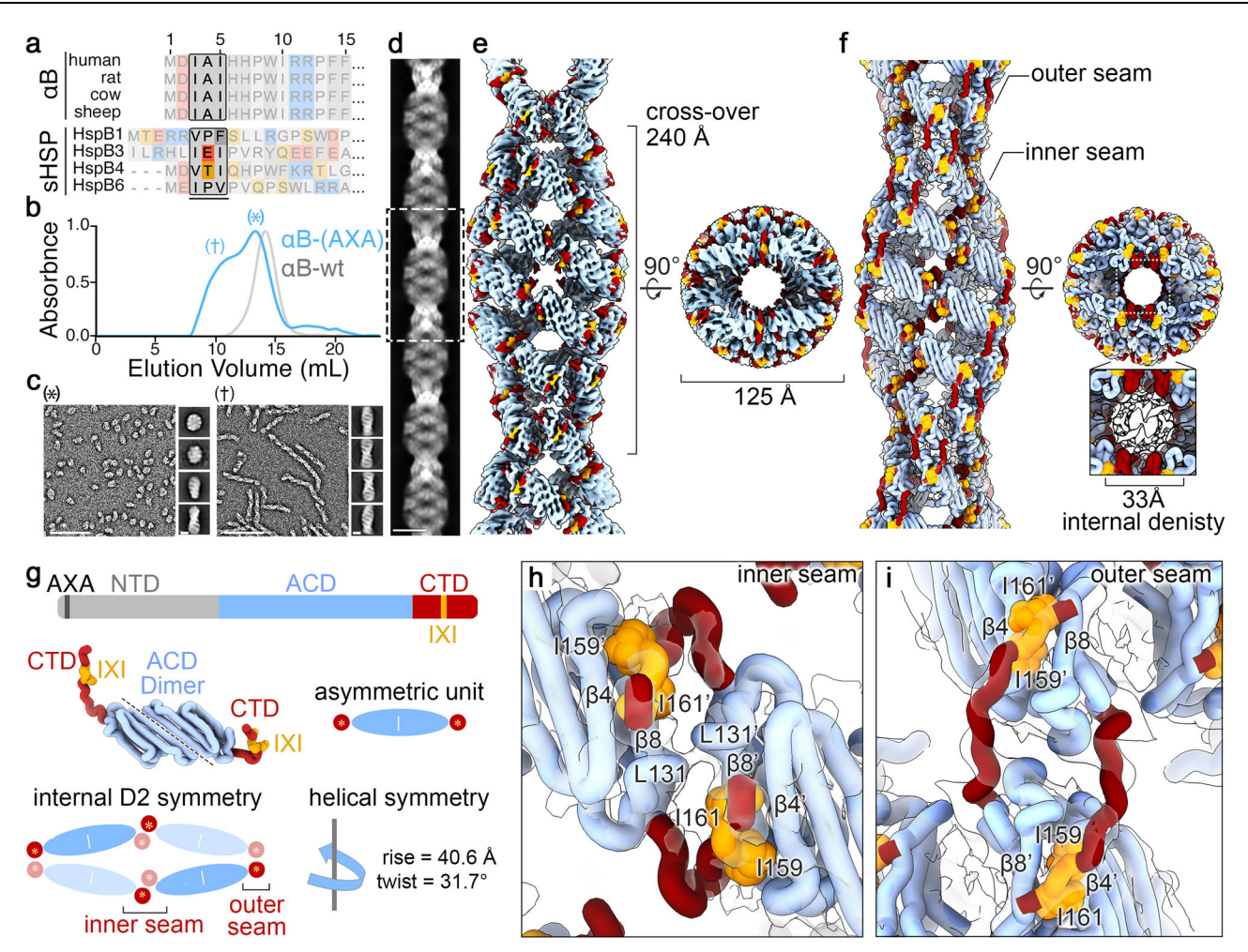


Fig. 1 | **αB-AXA fibril resolved by cryo-EM. a** Sequence alignment of the distal region of the N-terminal domain of αB -crystallin showing conservation of the NT-IXI motif (boxed) across model species that were mutated in this work (top), and putatively identified NT-IXI regions in other related sHSPs (bottom). Residues colored by amino acid properties (non-polar–gray, aromatic–dark gray, polar–orange, basic–blue, acidic–red). In canonical IXI-motifs, isoleucine may be replaced by valine. In other sHSPs, such as HSPBI, the NT-IXI motif may be more cryptic, with isoleucine positions replaced by other hydrophobic residues. **b** Size-exclusion chromatography (SEC) profile of αB -wt (gray trace) and αB -AXA (blue trace). Peak fractions are labeled as (†), indicating region containing fibrils and (*) with native-like assemblies. **c** Representative EM micrographs (scale = 100 nm) isolated by SEC fractions (*, left) and (†, right), selected from a dataset of n = 119 and

93, respectively. Insets show representative 2D classes (n = 100). **d** Montage of 2D classes obtained by cryo-EM (scale = 10 nm), selected from n = 150 classes, to represent the fibrillar morphology. **e** Cryo-EM density map of the α B-AXA fibril state resolved at 3.4 Å resolution and (**f**). atomic model displayed in cartoon representation, with the ACD in blue, CTD in red and CT-IXI in orange. **g** Illustration of domain organization, colored as in panel (**f**) with NTD colored in gray (top), structure and illustration of the asymmetric unit showing 2-fold internal pseudosymmetry of the ACD dimer (middle), and schematic illustrating the internal D2 and helical symmetries present in the fibril assembly (bottom). **h**, **i** Zoomed views of CT-IXI motif binding with the ACD β 4/8 groove at inner and outer seam, respectively. Cryo-EM density is displayed in transparency. Interacting residues between neighboring subunits are labeled.

due to the high-degree of flexibility at the c-terminus and were not modeled.

The fundamental building block of the αB -AXA fibril assembly is the ACD dimer, where each subunit adopts an expected IgG-like β -sandwich fold. In the resolved configuration, formation of the ACD dimer occurs through an in-register interface involving $\beta 6/7$ (aka the AP_{II} state)^{27,29,39}. The conformation of the ACD dimer closely resembles previously described structures obtained from diverse αB -crystallin constructs, particularly resembling the original ACD X-ray structure (PDB 2WJ7)²⁷, with an overall C α r.m.s.d. of -1.6 Å (Supplemental Fig. 5).

Further investigation highlights several structural features that have exhibited a variety of conformational states in previously described αB -crystallin ACD structures. The loop that links βS and βG is resolved adopting a so-called upward conformation. This conformation is supported by electrostatic interactions between D109 and R116 as well as R120 from the adjacent protomer, effectively

reinforcing the dimer interface (Supplemental Fig. 5). Genetic mutations affecting D109 and R120 have been linked to familial cataract and various myopathies $^{47-50}$. These mutations have been shown to alter the structural state of the αB -crystallin oligomer and have a negative impact on its chaperone function $^{51-54}$, underscoring a critical importance to maintaining the structural-functional integrity of the holocomplex.

Moreover, the $\beta 2$ strand and $\beta 2-3$ loop is resolved in the fibril morphology, but notably only for one of the protomers in the ACD dimer (*residues* 66–74 in subunit A, forming the outer seam), reflecting differences in the overall stability of this secondary structural element (Supplemental Figs. 1 and 5). The $\beta 2$ -strand is part of the 'boundary region', which has not been consistently resolved in various X-ray and NMR structures of the ACD^{27,36,39}. Here, the differences in conformational stability in this region could stem from the pseudo-symmetric relationship between the two protomers and

possibly coupled with differences in their interaction with NTDs, as further elaborated below.

In the context of the helical assembly, each ACD dimer is arranged with overall D2-symmetry (Fig. 1g), which establishes a two-start helical arrangement and leads to the rung-like features created by corresponding pairs of ACD dimers. The helical architecture generates an interior cavity with an approximate diameter of 5 nm that is filled with poorly defined density, presumably belonging to the NTD. The helical rise of 40.6 Å generates separation between the ACD rungs, resulting in the formation of ~20 Å wide fenestrations that are clearly resolved along the helical assembly (Fig. 1e, f). These features of the αB -AXA scaffolding bear a notable resemblance to the fenestrated cage-like architectures previously proposed from low-resolution cryo-EM models of wildtype αB - and αA -crystallins, and other sHSPs $^{40,42,55-58}$.

The CT-IXI forms multiple domain-swapping interactions with the ACD groove

The internal symmetry of the fibril assembly gives rise to two distinct interfaces formed between the ACD dimer building blocks, referred to as the inner and outer seam (Fig. 1f-i). The inner seam emerges from the pairing of ACD dimers that constitute the rungs of the assembly, which appear stitched together through domain-swapped CTDs exchanged between adjacent subunits (Fig. 1g, h). Conversely, the outer seam is formed along the edge of the filament, where ACD dimers are stitched together along the helical axis through domain swapped CTD interactions occurring between stacked subunits (Fig. 1g, i). As a result, this structural arrangement gives rise to two distinct conformational states adopted by the CTD.

In both scenarios, the domain swap interactions involve the participation of the conserved CT-IXI motif from one protomer and the hydrophobic groove generated by $\beta4/8$ from a protomer on a neighboring ACD. In the context of the inner seam, the CT-IXI is positioned such that I159 establishes interactions with residues V91, V93, and I133, while I161 interacts with L89, V91, L137, and L143 that form hydrophobic pockets within $\beta4/8$ groove (Fig. 1h and Supplemental Fig. 6). S135, situated within the ACD groove, lies between these two hydrophobic pockets, effectively bifurcating the two bound isoleucine residues. The resulting knob-and-hole interaction is analogous to previous structural studies of the αB -crystallin ACD bound to CTD-mimicking peptides 30,34 . Remarkably, the only other notable interaction stabilizing this interface occurs between symmetry-related residues L131, contributed by adjacent ACD domains (Fig. 1h).

In comparison, the CT-IXI interaction for the outer seam occurs in the opposite orientation with respect to the ACD. In this case, I159 inserts into the pocket formed by L89, V91, L137, and L143, while I161 engages with the pocket formed by V91, V93, and I133 (Fig. 1i and Supplemental Fig. 6). The flexibility of the linker connecting the ACD to the CT-IXI, coupled with the palindromic sequence within this region of the CTD, allows for a bidirectional orientation about the ACD. The CT-linker adopts a distinctive compact turn to facilitate the angle of approach for the inner-seam binding site. Conversely, the outer-seam interaction relies on a relatively extended conformational state for the CT-linker, positioning the IXI-motif against the interacting ACD $\beta4/8$ groove with a reversed orientation compared to the inner-seam interaction.

A quasi-ordered NTD buttresses the interior core of the ACD fibril assembly

The NTD is considerably less resolved in the cryo-EM map, as compared to the ACD and CTD domains, and appears as a quasi-ordered density that occupies nearly the entire interior cavity of the fibril (Fig. 2a). The high-order organization of the ACD dimers gives rise to two distinct electrostatic surface properties within the fibril assembly (Fig. 2b). The exterior surface, comprising $\beta 4$, $\beta 5$, and $\beta 6/7$ of the ACD

dimer, is relatively smooth and features an overall electronegative surface potential (Fig. 2b, c). In comparison, the interior surface of the helical assembly, composed of $\beta 3$, $\beta 8$, and $\beta 9$ of the ACD dimer, displays a mix of hydrophobic regions along with a distinctive positively charged groove formed by the ACD dimer interface (Fig. 2b, c). This internal ACD groove is occupied by a moderately well-resolved portion of the cryo-EM map attributed to a segment of the NTD (Fig. 2d, yellow). The interaction appears to be reinforced by the $\beta 2$ strand from subunit A of the ACD, which lays across the top of the NTD region, forming a lid-like feature that may further stabilize the ACD-NTD interaction (Fig. 2e, dark blue).

While the local resolution of the NTD segment bound by the ACD site was insufficient for unequivocal sequence assignment, it is recognized that a conserved hydrophobic region of the NTD has been implicated in binding to the ACD interior groove region in α -crystallins and other sHSPs (Fig. 2f and Supplemental Fig. 6) $^{36.59,60}$. We fitted this NTD region into the cryo-EM density, corresponding to αB -crystallin residues LFDQFFGE (residues 23-30) (Fig. 2d, zoom). This peptide region, known as the "conserved region" among sHSPs, contains several bulky hydrophobic sidechains (F24, F27, F28) that align with the cryo-EM map features and would closely interact with other hydrophobic residues constituting the ACD groove (e.g., F84, F118, and H83). However, due to the uncertainties associated with limited resolution, this sequence assignment remains tentative and was fit as poly-alanine in our final model.

The rest of the NTD is characterized by poor resolvability in the cryo-EM map that may reflect inherent disorder or the assumption of multiple quasi-ordered conformational states. These states, despite substantial efforts employing various image processing techniques, could not be fully resolved or differentiated by image classification routines. In a broader context, these observations implicate a critical role of the NTD in buttressing the overall architecture of the ACD core assembly, which is otherwise supported by domain swapped CTD interactions that are interconnected solely through flexible linkers.

αB -AXA fibril state retains a high-degree of conformational plasticity

Initial attempts at refinement of the α B-AXA fibril structure yielded 3D reconstructions with limited resolutions, in the range of ~6-8 Å (Supplemental Fig. 3). It was suspected that this limited resolution might be attributed to the presence of long-range conformational heterogeneity. This notion was supported by observation that fibrils exhibit a substantial degree of flexibility, as evident from low-magnification images (Supplemental Fig. 2). To quantitatively evaluate this morphological flexibility, image segments were extracted from the cryo-EM dataset using large box sizes, sufficient for sampling at least two cross-over points (or one complete helical period) and subjected to 2D classification analysis (Fig. 3a, c). Measurement of cross-over distances resolved in the 2D classes revealed significant variation, falling within the range of approximately 230-245 Å or a variance of approximately 30 Å per helical period. At a short-range level, this distribution indicates a variation in rung-to-rung distances of only ~1.0-1.5 Å. Likewise, distinct variability along the principal helical axis is evident in the 2D class averages, manifested with bend angles ranging from 0° to approximately ±20°, as measured over a single helical period. This conformational heterogeneity was also identified and visualized using 3D Variability Analysis (3DVA) in cryoSPARC⁶¹, which illuminated two primary components of structural variability characterized as a combination of stretching and bending modes (Fig. 3b, d; Supplemental Fig. 7; and Supplemental Movie 2). These analyzes underscore the significant conformational plasticity that is retained by the helical assembly, congruent with the flexibility of the linkers connecting the ACD and CTD and the quasi-ordered nature of the NTD that reinforces the interior of the fibril architecture.

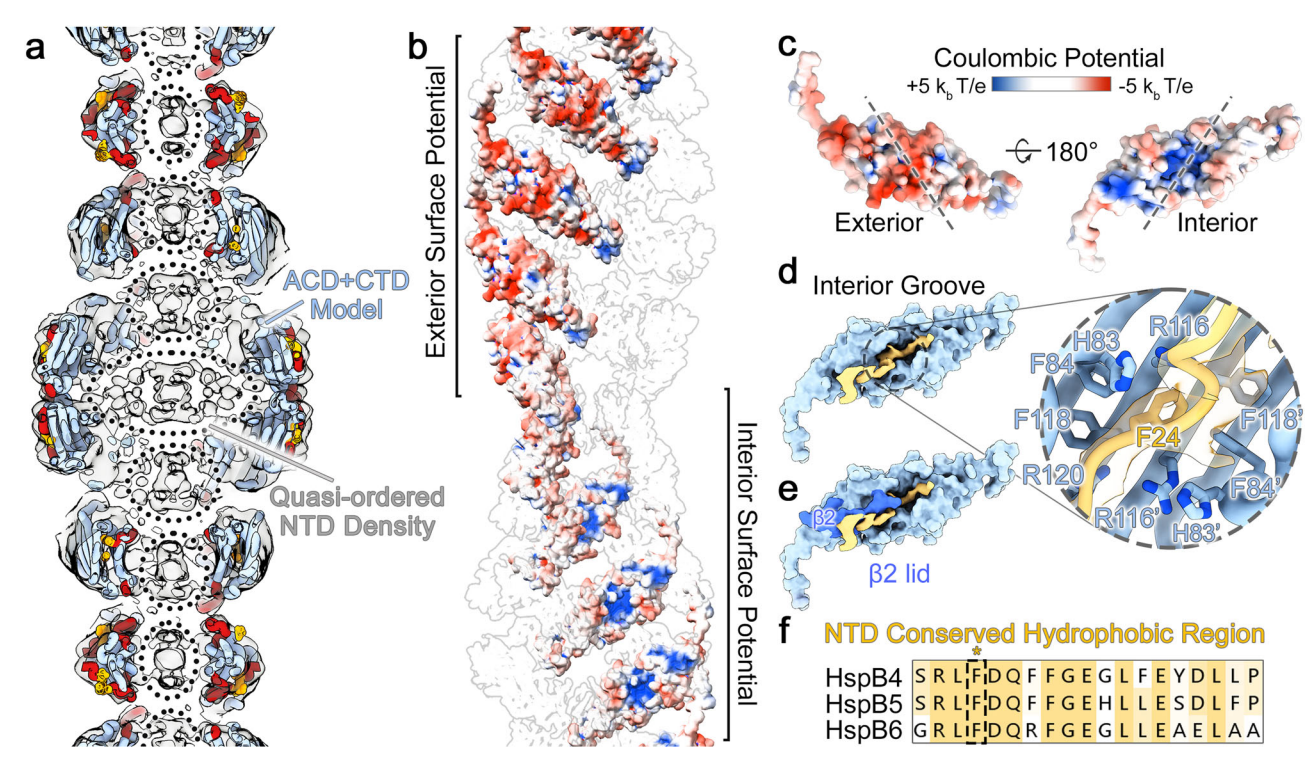


Fig. 2 | The quasi-ordered NTD fills an internal cavity of the αB-AXA fibril and forms interactions with the ACD. a Cut-away view showing αB-AXA fibril model colored as in Fig. 1, with the cryo-EM density map overlayed in gray. The unmodeled density filling the interior cavity of the fibril is assigned to the NTD (dotted circles). **b** Electrostatic surface representation of αB-AXA fibril, with only a single filament stand displayed for clarity (red: -5 kb T/e, white: 0 kb T/e, blue: +5 kb T/e). **c** Electrostatic surface representation of a single αB-AXA subunit, oriented with exterior surface (left) and interior surface (right). The ACD dimer interface is indicated by dotted lines. The β2 strand is omitted for clarity. **d** Surface representation of the ACD dimer (light blue) and segmented cryoEM map showing a

region of the NTD (yellow) bound within the interior groove of the ACD. This density is putatively assigned to a conserved hydrophobic-rich region of the NTD (residues 20-32). Zoom view shows a C α trace fit into the putative NTD density with a conserved F24 residue displayed. Residues from the ACD that interact with this peptide region also displayed and labeled. **e** Same as panel (**d**) with surface representation of the β 2 strand resolved in a single protomer (dark blue) that forms a lid covering the bound NTD region. **f** Sequence alignment of the putative NTD peptide binding region, showing conservation of hydrophobic-rich region with phenylalanine (F24) boxed.

αB-AXA fibrils are temperature dependent and reversible with native-like caged oligomers

As described above, during the purification of αB -AXA from bacterial expression, a mixture of native-like oligomers and helical fibril states was obtained. Upon further investigation, it was noted that when the purified mixture was incubated at room temperature, a gradual transformation into the fibril state occurred. We aimed to comprehensively characterize this phenomenon by closely monitoring the transition between native-like oligomers and helical fibril morphologies, using dynamic light scattering (DLS) and by direct visualization using EM at varying incubation temperatures.

To exemplify this characterization, we considered the case of starting with a sample exclusively composed of fibrils, obtained via SEC separation from the initial mixture. These fibril structures remained stable for several days at room temperature in a standard buffer at pH 7.4, containing 150 mM NaCl and 1 mM EDTA (the same buffer utilized for structural analysis). However, when subjected to a temperature ramp ranging from 25° to 45° C over a span of 60 minutes (~0.33°C per minute), the sample readily converted into a relatively uniform population of globular native-like assemblies (Fig. 3e, f). Under these conditions fibril disassembly occurs rapidly (<10 min), with initial disassembly beginning at ~37°C, with an apparent 50% transition at ~40° C and complete conversion occurring at a temperature of ~42° C.

The observed transformation was found to be fully reversible, albeit with significantly distinct kinetics. Following conversion to native-like oligomer assemblies, the same sample could be readily transformed back to the fibril state through incubation at room

temperature (Fig. 3g). This process of fibril reassembly occurred over a span of several days, typically reaching completion after 3–4 weeks. Notably, fibrils formed during incubation were markedly longer than those initially isolated from bacterial expression (reaching >1 μm in size), with otherwise identical apparent morphology. This reversible transformation process served as the basis for preparing samples for high-resolution cryo-EM analysis, described above.

Following this procedure, fibril disassembly could be further repeated, with samples readily converting back to native-like oligomeric structures at an incubation temperature of 42° C (Fig. 3g). Single-particle analysis of the thermally-converted oligomeric state imaged by negative-stain EM showed morphological features that were generally consistent with wild-type particles but with slightly larger and more irregular oligomeric features, consistent with the disruption of key protein-protein interactions (Supplemental Fig. 8). Notably, 2D class averages from this dataset lacked evidence of any significant population of fibrils/protofibrils, confirming morphological transition to the native caged-like assembly.

Disrupting the NT-IXI motif reduces chaperone potency and potentiates client-induced co-aggregation

Previous studies have suggested a role for the NT-IXI motif in αB -crystallin in client binding interactions³⁸. To address the potential functional effects of disrupting the NT-IXI motif, we leveraged the temperature dependence of the fibril and native-like oligomer states to assess the impact on chaperone function (Fig. 4). Chaperone activity was gauged by monitoring the suppression of light scattering aggregation during the chemically-induced unfolding of a model client,

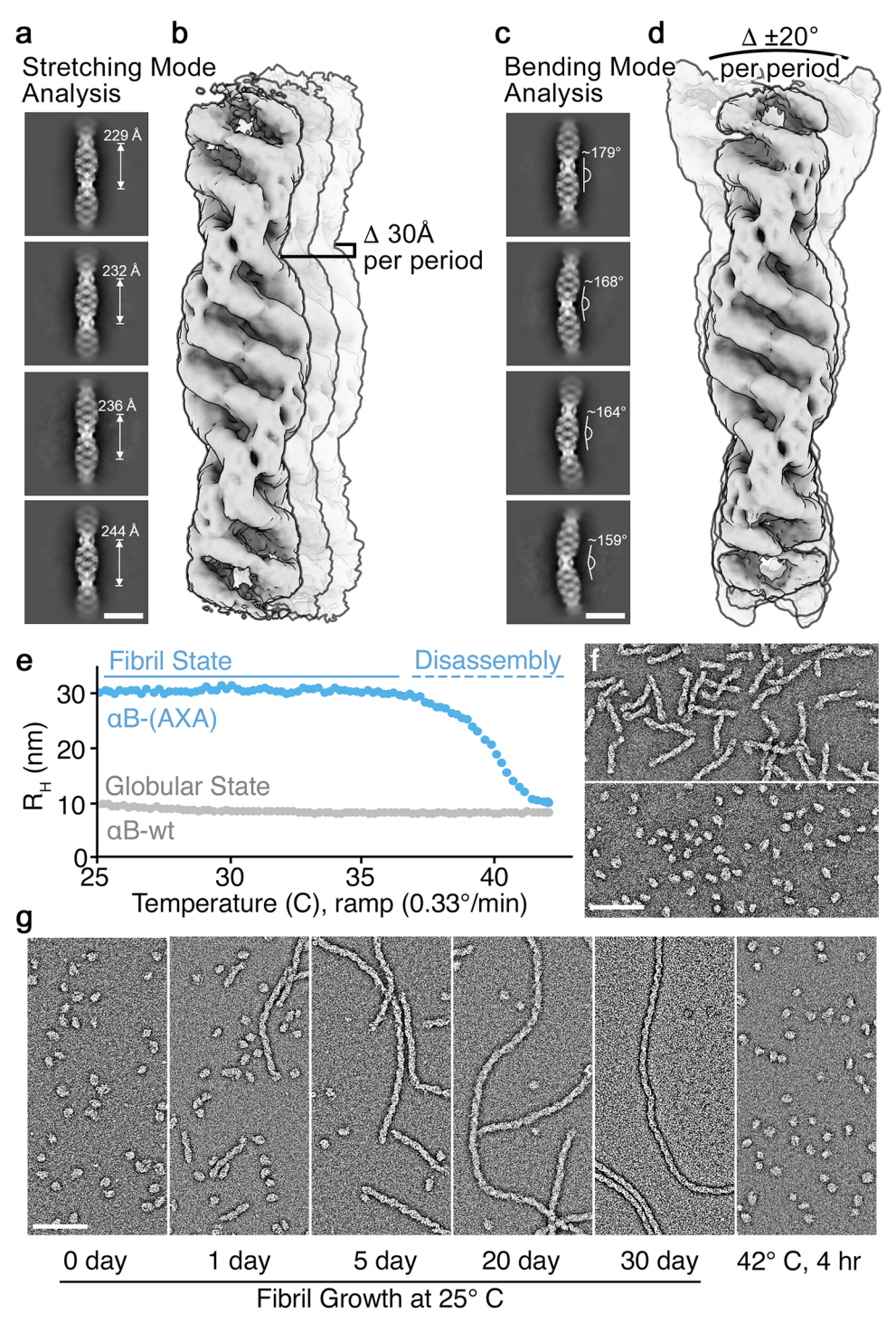


Fig. 3 | α**B**-AXA fibrils display structural plasticity and temperature-dependent reversibility with the native-like oligomeric state. a Representative 2D class averages of αB-AXA fibrils obtained by cryo-EM showing variability in cross-over distances with measurements labeled (scale = 20 nm). **b** Overlay of cryo-EM maps obtained from one of the primary principal components obtained by 3D variability analysis in cryoSPARC⁶¹, illustrating a stretching mode. A range of -30 Å indicates the variability of fibril length per helical period, as measured in 2D class averages. **c** Representative 2D class averages showing variability in bend angles with measurements labeled (scale = 20 nm). 2D classes in panels a and c were selected from a dataset of 200 classes, and measurements were made from 10 classes for each mode. **d** Overlay of cryo-EM maps obtained from one of the primary principal components obtained by 3D variability analysis, illustrating a bending mode. A range of bend angles of -20° per helical period is indicated, as measured from the 2D class averages. Cryo-EM maps in panels (**b** and **d**) were aligned to the bottom

rung density of the fibril for visualization purposes. **e** Reversibility of αB -AXA fibrils demonstrated by conversion to the native-like globular state by monitoring the change in hydrodynamic radius (R_H) measured by dynamic light scattering as a function of temperature (°C). αB -wt did not show appreciable changes in R_H (gray trace) over temperature range of 25 – 45° C. **f** EM micrographs of negatively stained specimens showing the starting αB -AXA fibrils (top) and resulting conversion to native-like oligomeric assemblies following heat ramp to 45° C (bottom). **g** Native-like oligomers (left) were then incubated at room temperature (25° C) and shown to slowly convert back to the helical fiber state over a period of -30 days (middle panels), as monitored by EM. Grown fibrils were then readily converted back to native-like oligomers upon incubation at 42° C for four hours (right). Scale bars = 100 nm, in panels (**b**, **c**). Micrographs in panels (**f** and **g**) were representative of at least 3 independent observations.

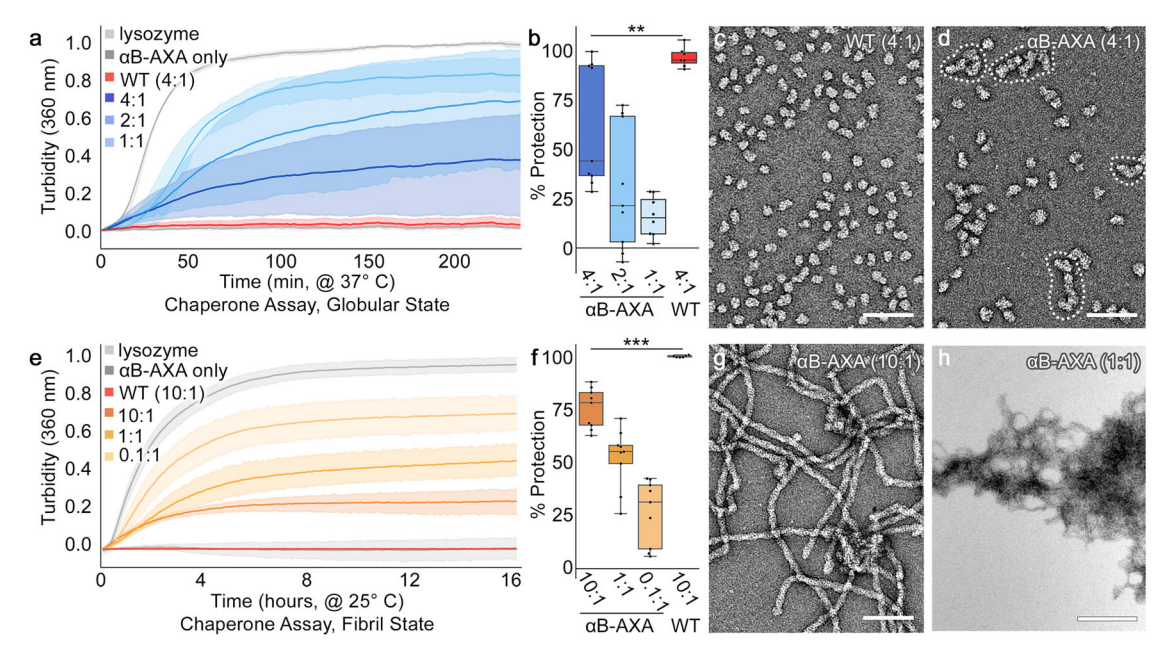


Fig. 4 | Disruption of the NT-IXI motif results in reduced chaperone activity in both native-like globular and fibril states. a Chaperone assays against unfolding lysozyme client conducted with varying molar ratios of αB -AXA in the native-like globular state (blue traces), as monitored by light scattering (turbidity) at 360 nm at 37° C as a function of time (hours). Lysozyme-only (10 µM, light gray trace) and αB-wt (40 μM, dark gray trace) were run as positive and negative controls, respectively. αB-AXA prepared at 1:1, 2:1 and 4:1 (chaperone:client) molar ratios. Data are normalized to lysozyme-only conditions. Each condition contained 3 biological replicates, conducted with 1-3 technical replicates (n = 7-9). Standard error of the mean (s.e.m.) shown with semi-transparent shading. b Percent protection versus untreated lysozyme summarized in box plot representation and colored as in panel a. Statistical significance (p = 0.0079; **), calculated from all replicates using a two-tailed t-test. c. d Representative electron micrographs of endstate reactions for the 4:1(chaperone:client) ratios obtained for αB-AXA and αB-wt, respectively. Scale bar = 250 nm. αB-AXA chaperone/client complexes appear as more irregular and elongated particles (dotted outlines), as compared to αB-wt under these same conditions (see also, Supplemental Fig. 9). e Chaperone assay of

αB-AXA in the fibril state conducted at 25° C (orange-yellow traces). Lysozyme-only (10 μ M, light gray trace) and α B-wt (40 μ M, dark gray trace) were run as positive and negative controls, respectively. αB-AXA prepared at 0.1:1, 1:1 and 10:1 (chaperone; client) molar ratios. Due to limited sample, each condition contained 1-3 biological replicates, conducted with 1-6 technical replicates (n = 6-9). Standard error of the mean (s.e.m.) shown with semi-transparent shading. f Percent protection summarized in box plot representation and colored as in panel (e). Statistical significance ($p = 5.4 \times 10^{-5}$; ***), calculated from all replicates using a two-tailed t-test. g, h. Representative electron micrographs of end-state reactions for the 10:1 and 1:1 (chaperone:client) ratios obtained for αB-AXA fibril state, respectively. Scale bar = 250 and 500 nm in panels (g and h), respectively. Increasing client ratios correlate with an increase tangling and/or co-aggregation of αB-AXA fibrils. Box plots show the central 50% of the data, spanning from the first quartile (Q1) to the third quartile (Q3), with a line at the median. Whiskers extend to the minimum and maximum values. Micrographs are representative of at least 3 independent observations. Source data are provided in a Source Data file.

lysozyme¹⁶. In each experiment, lysozyme (10 μ M concentration) was prepared in our standard pH 7.4 buffer, complemented with 150 mM NaCl and 1 mM EDTA, and unfolding of lysozyme was triggered by addition of reducing agent (1 mM TCEP) and monitored by light scattering at 360 nm. This was performed either without chaperone (negative control) or with varying amounts of α B-AXA. For comparison, α B-wt was tested under identical conditions as a positive control.

To evaluate the NT-AXA variant within the context of the native-like oligomer, samples were fully converted to this state by preincubating at 42° C, then sustained in this state at an incubation temperature of 37° C. At this temperature, reduced lysozyme shows robust and consistent aggregation kinetics (Fig. 4a, *light gray*). When combined at a 4:1 stoichiometric ratio (40 μ M chaperone), α B-wt effectively inhibits light-scattering aggregation (96.7% \pm 1.9 protection) (Fig. 4a, *red*). At the same 4:1 ratio, the α B-AXA variant in the native-like oligomer state was significantly less effective (62.0% \pm 10.3 protection, p < 0.05) (Fig. 4a, b, *dark blue*). The suppression of aggregation further diminishes at lower chaperone:client ratios, and at a 1:1 ratio the α B-AXA variant displayed only modest protection (16.1% \pm 3.6) (Fig. 4a, b, *light blue*).

A morphological comparison by EM conducted on the 4:1 reactions highlight the differences in chaperone efficacy between αB -wt and αB -AXA oligomers (Fig. 4c, d and Supplemental Fig. 9). We have demonstrated in previous work that under conditions where αB -wt offers complete protection from aggregation, the resultant

chaperone-client complexes bear a close resemblance to the apostate¹⁶. This finding is corroborated in our current study (Fig. 4c). In contrast, αB -AXA/client complexes, when examined at an identical 4:1 stoichiometric ratio, manifest a more irregular and notably elongated morphology (Fig. 4d). Such elongated chaperone-client forms have been demonstrated for αB -wt in scenarios where its chaperone capacity is challenged¹⁶. Morphological comparisons are varying chaperone:client ratios are congruent with reduced chaperone capacity of αB -AXA in the oligomeric state and the potentiation of client-induced co-aggregation states (Supplemental Fig. 9).

Together, these observations suggest that while the NT-IXI motif isn't essential for chaperone activity, its alteration significantly impacts chaperone efficacy, consistent with the proposed role of the NT-IXI in client recognition and/or binding. The morphological analysis further supports the idea that the helical state induced in the αB -AXA variant may mirror aspects of client-induced elongation of αB -crystallin, as suggested by their similar morphological features, including comparable average diameters (~13 - 16 nm) and apparent flexibility. Although the client-induced state of αB -crystallin lacks helical features, the underlying propensity for directional elongation may be reflected in the αB -AXA variant (see Discussion).

Next, to assess chaperone activity of the αB -AXA variant in its helical fibril form, we repeated the aggregation suppression assay at 25 °C, where the fibril structure remains stable. While lysozyme unfolding kinetics decrease considerably at this temperature, they

remained robust and consistent, as observed by monitoring light-scattering (Fig. 4e, *light gray*). Remarkably, even in its fibril form, αB -AXA retains appreciable chaperone activity, though apparently significantly reduced compared to wildtype. At the highest tested chaperone concentration, 10:1 stoichiometric ratio (chaperone:client), αB -AXA fibrils appear to suppress only 75.4% \pm 3.1 of aggregating lysozyme activity (Fig. 4e, f, *yellow*). Conversely, αB -wt exhibits nearly total protection under identical conditions (99.9% \pm 0.2 protection) (Fig. 4e, f, *red*). It's worth highlighting that at a 1:1 ratio αB -AXA fibrils still offer significant protection, reducing aggregation by 52.1% \pm 4.7 (Fig. 4e, f, *orange*) and remarkably, at a 0.1:1 ratio a protection of 26.4% \pm 5.1 is still present (Fig. 4e, f, *dark orange*).

Morphological evaluation of chaperone reactions with αB-AXA fibers unveiled complex behaviors. In scenarios where αB-AXA fibers were most effective (10:1 ratio), fibril morphology largely resembles the apo-state, albeit with the appearance of some induced fibril clustering (Fig. 4g). More intriguingly, under higher client ratios (e.g., 1:1 ratio) extensive fibril clustering is observed (Fig. 4h). EM images showed massive fibril tangles, some spanning up to 2-3 µM in diameter. Such large aggregates would be sufficient to contribute to light scattering at 360 nm, used for monitoring chaperone activity, complicating interpretation of the aggregation suppression assay. Nevertheless, it is evident that 1) αB-AXA fibrils retain some degree of chaperone activity, and 2) client-interaction with the α B-AXA fibrils induces co-aggregation in this system. A possible interpretation of these results is that the unfolded client gets recognized and simultaneously tethered to multiple fibrils, triggering fibril cross-linking and co-aggregation. However, as the unfolded client is not resolved in the EM images, further studies are needed to confirm this proposed model.

Discussion

Our study underscores the critical role of the NT-IXI motif in the structural and functional dynamics of the α B-crystallin sHSP chaperone. By disrupting the competitive interaction between the NT-IXI and CT-IXI motifs at the ACD \(\beta 4/8 \) hydrophobic groove, we observed a significant shift in αB-crystallin's assembly equilibrium, favoring the formation of a helical fibril state. Interestingly, this fibril formation aligns with similar observations in distantly related sHSPs such as AgsA in Salmonella, which forms heat-inducible fibrils to prevent irreversible aggregation⁶², and HSP20-3 in the tardigrade Ramazzottius varieornatus, where filaments confer chaperone activity and proposed to contribute to desiccation tolerance⁶³. Notably, such physiological filamentous states have not been previously documented in vertebrates to the best of our knowledge. While the fibril state of αB crystallin observed in our study stems from the non-physiological perturbation to the NT-IXI motif, we suggest several functional and mechanistic insights that can be gleaned.

Despite advancements in structural biology, a high-resolution model of full-length αB-crystallin in its native oligomeric state(s) has remained elusive, limiting studies to pseudo-atomic models of its 24meric cage-like structure derived from hybrid methods and predictive modeling^{24,41}. While the NT-AXA variant induced a distinct quaternary assembly, the high-resolution depiction may provide both clarity and depth to understanding the principles of αB -crystallin oligomerization. The ACD dimer functions as the foundational unit in both the fibril and native oligomeric states⁴¹. Previous studies on truncated αB-crystallin, which included only the ACD, revealed multiple potential registers (AP_I, AP_{II} and AP_{III}) at the dimerization interface. In the context of the fibril state, the full-length αB -crystallin is resolved only in the AP_{II} register, consistent with solid-state NMR data obtained on the fulllength αB-crystallin oligomer³⁹. Despite exploring the possibility of alternative registers in the αB-AXA fibril through extensive 3D classification, we found no evidence supporting their significant presence. Our structural results suggest the AP_{II} register is stabilized through interactions between the NTD peptide and the ACD's interior groove, as such interactions would be incompatible with alternative registers, indicating a specialized role of the 'conserved region' of the NTD in stabilizing this specific state.

The structural role of the NTD has remained the most enigmatic region of αB-crystallin. Pseudo-atomic models have been proposed. where the NTD contributes to the symmetric lateral packing of ACDs, forming the exterior scaffold of the caged assembly^{24,41}. In the NMRbased model, only the proximal portion of the NTD (residues 1-39) is positioned towards the interior cavity²⁴, whereas in the cryo-EM based model the NTD was completely excluded from the interior cavity⁴¹. A similar structural context of the NTD has been also proposed in a cryo-EM based pseudo-atomic model of the related αA-crystallin⁴². In contrast to these proposed models, in the fibril morphology induced by the αB-AXA variant, the entire NTD (residues 1–62 chain A; 1–75 chain B) is sequestered within the internal cavity of the assembly, adopting a quasi-ordered or partially disordered state. This localization and quasiordered nature of the NTD remains consistent with observation from these and other earlier studies: solid-state NMR data indicated the NTD can adopt multiple conformational states^{36,39}, while cryo-EM reconstructions have shown only weakly defined or indiscernible density within the interior of native assemblys^{13,40,41,56}. Furthermore, cysteine crosslinking that has been shown to occur between subunits at residues A57, S59 and T63 are also consistent with the expected close interaction of NTDs from multiple subunits²⁴. Internalization of the NTD in the αB -crystallin fibril also aligns with observations of other high-order sHSP oligomeric structures characterized in other organisms at higher resolutions 55,64,65.

In the αB-AXA fibril structure, a segment of the NTD was partially resolved, anchored by binding interactions along an interior groove at the ACD dimer interface (Fig. 5). While the local resolution was insufficient for confident assignment, the characteristics of this region are in line with a conserved hydrophobic region known to interact similarly with the ACD in other sHSPs^{36,59,64} (Fig. 2d and Supplemental Fig. 1). This interaction mirrors findings from a crystal structure of a full-length sHSP from C. elegans, Sip1, where a hydrophobic region of the NT lines this same interior groove⁶⁵, as well as a recent crystal structure of the HSPB2/3 heteromeric complex, where a density along the ACD groove, likely belonging to the NTD, was observed but could not be distinctly assigned due to limited resolution⁶⁶. In the fibril state, this interaction is further supported by extensive contact with the $\beta2$ strand, which acts as a 'lid' that effectively encapsulates this portion of the NTD within the ACD dimer interface, enhancing the localized stability of this interaction. Notably, the β2 strand displays considerable conformational flexibility, often unresolved in various αB -crystallin ACD structures 27,36,39 . In the fibril assembly, the β2 'lid' is asymmetrically resolved, appearing only in subunits along the external seam and less well-defined than other ACD regions, reinforcing its role as a dynamic element of αBcrystallin.

The interaction between the NTD and ACD of αB -crystallin likely extends beyond merely contributing to architectural stability and high-order assembly^{27,67}. Areas of the ACD that interact with the NTD peptide are crucial for client recognition and chaperone activity⁶⁸, particularly the mini-chaperone peptide region (residues 73–92)⁶⁹. Under basal conditions, the NTD-ACD interaction obscures this critical client-recognition site, and thus may serve to conceal this site for activation. Genetic deletion of the conserved NTD segment proposed to bind the ACD not only disrupts high-order assembly and reduces structural stability but also increases surface hydrophobicity and enhances the chaperone activity of αB -crystallin⁷⁰. Furthermore, several phosphorylation sites situated within the NTD may effectively disrupt this NTD-ACD interaction. Such a modification would likely lead to oligomer destabilization, exposure of the client-binding site, and activation of chaperone function²¹.

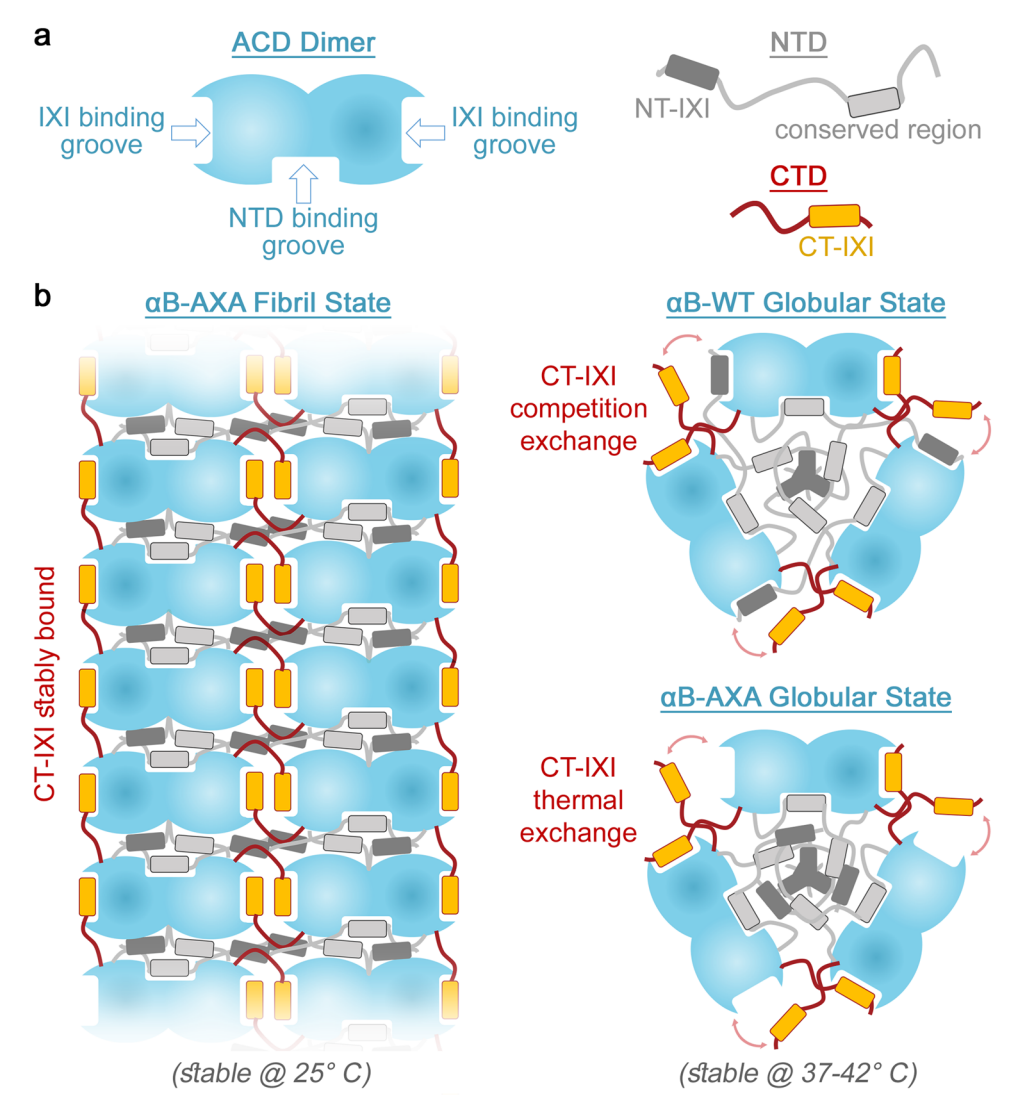


Fig. 5 | **Overview and proposed structural organization of αB-crystallin in fibrillar and globular states.** a Illustration depicting the α B-crystallin ACD dimer building block (blue) that establishes two hydrophobic IXI-motif binding grooves and a putative NTD binding groove at the dimer interface. The NTD (gray) comprises two conserved regions, the NT-IXI motif (dark gray box) and a conserved hydrophobic region (light gray box). The CTD (red) contains the conserved CT-IXI motif (orange box). **b** When the NT-IXI is ablated (α B-AXA), the CT-IXI can form persistent and stable interactions with the IXI binding grooves in the ACD, promoting elongated fibril assembly. In this state, the NTD is buried within the interior

cavity of the assembly. The NTD binding groove of the ACD is occupied and is presumed to correspond to the conserved region of the NTD. Upon heating the αB -AXA construct from 25 °C to 37–42 °C, the structure transitions into a globular state resembling wild-type αB -crystallin (αB -WT). This transformation is proposed to result from thermal energy causing rapid exchange of the CT-IXI with the ACD IXI-binding groove, mimicking the exchange mechanism proposed in αB -WT, where both the CT-IXI and NT-IXI undergo competition exchange for a limited number of binding grooves in the ACD.

The CTD of αB -crystallin is recognized for its dynamic nature, posing challenges in precisely defining its multiple modes of interaction with the ACD within high-order oligomeric structures, as reflected by the differences in previously proposed pseudo-atomic models^{24,41}. In the αB-AXA fibril state, the intrinsic flexibility of the CTD linker serves two critical functions. First, it accommodates multiple conformational states, facilitating domain-swap interactions among neighboring ACD dimers through hydrophobic knob-in-hole engagements involving the conserved CT-IXI motif and the ACD $\beta 4/8$ groove. The palindromic sequence surrounding the CT-IXI motif also allows for a bi-directional orientation of the CTD within the ACD edge-groove. Secondly, this flexibility imparts long-range structural plasticity to the assembly, a feature expected to be essential for adopting various oligomeric states and accommodating diverse clients^{71,72}. Notably, in the fibril-state, the highly charged C-terminal extension following the IXI motif, while not resolved in our cryo-EM reconstruction, is oriented

toward the oligomer's exterior, aligning with its expected role in enhancing solubility.

The NT-AXA variant of αB -crystallin exhibits a remarkable ability to reversibly transition between fibrillar and globular oligomeric states. We hypothesized that the competition between NT-IXI and CT-IXI for the ACD $\beta 4/8$ groove contributes to αB -crystallin's polydispersity³6. In the αB -AXA variant, unrestricted access of CT-IXI to the ACD binding site indeed promoted a more monodispersed structure, shown to be the elongated fibril state. We suggest that elevated temperatures may increase the dissociation rate of CT-IXI, simulating rapid-exchange dynamics seen under native conditions¹9,24, and potentially facilitating a return to the globular state (Fig. 5). The mechanism of this transition, however, remains to be elucidated. For example, fibril formation might involve internal conversion of subunits within already formed oligomers, with elongation occurring through interactions with other converted oligomers. Alternatively, fibril

formation may occur de novo, mediated by subunit exchange events that seed fibril formation and elongation $^{17-20}$. The observation of small fibrillar species (or protofibrils) on the order of size of the native-like oligomers is consistent with either mechanism (see 2D class averages in Fig. 1c). Never-the-less, this capacity for reversible conversion between oligomeric and fibril states underscores αB -crystallin's ability to dramatically transform between quaternary states with only minor structural or environmental changes.

It also remains uncertain, why other sHSPs lacking an NT-IXI motif do not form fibrillar structures. Moreover, we found that mutational ablation of the NT-IXI motif from the close paralog, αA -crystallin, also did not result in the formation of fibrils under similar conditions shown for αB -crystallin (Fig. 1a and Supplemental Fig. 2). One explanation for this observation is that the CTD of αA -crystallin (and other sHSPs) lacks the palindromic sequence that surrounds the CT-IXI motif in αB -crystallin, likely to be crucial for forming the symmetrical lattice necessary for ordered helical assembly. Moreover, despite the similarities between αA - and αB -crystallin, these isoforms exhibit distinct oligomeric states, degrees of polydispersity, and dynamics $^{14,16,73-75}$ — highlighting their distinct complexities. Indeed, each sHSP has distinct structural and dynamic properties, finely tuned to their physiological roles, emphasizing the need for individual characterization and understanding.

While the fibril structure of the αB -AXA variant of αB -crystallin highlights key aspects of high-order sHSP assembly, the potential physiological relevance of this state remains unclear. We hypothesize that this structure may exemplify αB -crystallin's propensity to adopt highly elongated assemblies that are integral to its chaperone function. This is supported by our recent findings on a client-driven elongation mechanism in the α -crystallins¹⁶ (see also Fig. 4d). Similar elongated structures have been observed in native α -crystallin from aged lens tissues⁷⁶ and in other sHSP/client co-aggregates^{77,78}. The NT-IXI motif plays a role in client binding and is shown to become protected from proteolysis in the presence of substrate^{38,79}. The diminished chaperone activity of the αB-AXA variant in its native-like globular state, further underscores its role in modulating client interactions. Client engagement would effectively sequester the NT-IXI and eliminate its competition with the CT-IXI for ACD binding. The resultant elongated morphologies induced by client binding in αB-crystallin, although lacking helical symmetry, share gross morphological features with the αB-AXA fibril state, and underscore the native propensity for directional elongation of the sHSP scaffold. Further studies aimed at disentangling the complex dynamics and chaperone mechanism of the sHSPs will be needed to fully address this hypothesis and fully elucidate the implications of these findings.

Methods

NT-IXI motif identification, construct design and protein purification

The NT-IXI motif was identified by aligning the amino acid sequences of α -crystallins and other related small heat shock proteins. To generate the NT-AXA variant, site-directed mutagenesis was performed on a pET plasmid containing the human α B-crystallin gene, where residues I3 and I5 were replaced with alanine using the Quick-Change Lightning kit following the manufacturer's instructions (Agilent). Following mutagenesis, modified plasmids were introduced into XL-10 Gold cells for amplification. Plasmid DNA was then extracted using Promega miniprep kits and sequenced to confirm the introduction of the desired mutations.

For protein expression, DNA plasmids were transformed into BL21 $\it E.~coli$ cells, by heat shock at 42° C for 45 seconds. Cells were cultured in LB media at 37 °C under ampicillin control until they reached an optical density (OD) of 0.5. The culture temperature was then reduced to 18° C, followed by induction with 1 mM IPTG for protein expression overnight (~18 hours). Cells were harvested by centrifugation and the

pellet was re-suspended in 4 mL of lysis buffer containing 20 mM Tris pH 8, 1 mM EDTA (4 mL per gram of pellet) and stored at -80° C for subsequent protein purification.

Cell suspensions were thawed and treated with 0.1 mM DTT and PMSF, and lysis was carried out by sonication (Fisher Sonic Dismembrator), with settings at 70% intensity and pulse times of 30 seconds, for a total duration of 6 minutes. After sonication, an additional 0.1 mM PMSF was added to the lysate to prevent proteolytic degradation. The lysate was then ultra-centrifuged at 147,000 x g for 30 minutes at 4° C to remove insoluble cellular components. The supernatant was retained and further treated with 20 units of DNase I to degrade residual DNA. Following DNase treatment, the lysate was filtered through a 0.45 μm filter.

For protein purification, the clarified lysate was applied to a Sephacryl 300 column (Cytiva Life Sciences) that had been pre-equilibrated with a salt-free size-exclusion chromatography (SEC) buffer (20 mM Tris at pH 8.0, 1 mM EDTA, and 0.1 mM DTT). Fractions containing the αB -crystallin were identified by SDS-PAGE, pooled, and supplemented with 0.1 mM DTT. Pooled fractions were then loaded onto a MonoQ ion-exchange column (Sigma-Aldrich) and eluted across a salt gradient of 0.5 M NaCl. Elution peaks containing αB -crystallin were collected, pooled, and subsequently dialyzed with a 3.5 kDa molecular weight cut-off (m.w.c.o.) membrane (SnakeSkin, Thermo Scientific) against the final reaction buffer (20 mM HEPES, 100 mM NaCl, 1 mM EDTA, pH 7.4).

For comparison, an NT-AXA variant of human αA -crystallin was generated by replacing residues V3 and I5 with alanine, expressed in E. coli, and biochemically purified using the same methodology and purification procedures described above for αB -crystallin, with the exception of the final step. After determining that purification of the αA -AXA variant did not produce observable filaments, the buffer exchange was performed using a Super 6 increase column (Cytiva Life Sciences) equilibrated in the final reaction buffer (20 mM HEPES, 100 mM NaCl, 1 mM EDTA, pH 7.4).

Temperature dependence assays by DLS and EM

To elucidate the transitions between fibrillar and globular assemblies, samples were incubated at varying temperature and monitored by dynamic light scattering (DLS) and electron microscopy (EM). DLS assays were performed on a Wyatt DynaPro III instrument, with the resulting data processed using the DYNAMIC 6 software package. For initial characterization, protein samples were subjected to a range of temperatures, including 4° C, 25 °C, and 42° C. For temperature ramp assays, samples were started at 25° C and progressively heated to 60° C (0.33°/minute), beyond which point irreversible aggregation was observed. Morphological transitions were detected by DLS and subsequently confirmed by EM.

Extended incubation at 25° C produced samples with long, well-ordered fibrils. Full conversion to the fibril state was observed after incubations of up to 4 weeks, as confirmed by EM. Following this incubation period, samples used for structural analysis by cryo-EM underwent an additional step of dialysis to remove trace amounts of unconverted globular oligomers using a dialysis membrane with a 1 MDa m.w.c.o. (Repligen Spectra/Por, Spectrum Chemicals) and stored at 4° C.

Negative Stain Electron Microscopy

Negatively stained samples were prepared similarly for all specimens for EM analysis by placing $3\,\mu\text{L}$ drops of the protein solution onto carbon-coated copper mesh grids at approximate monomer concentrations of 720 nM. After a brief incubation period, excess solution was blotted away on filter paper, washed three times with water, stained with 0.75% uranyl formate (SPI-Chem), and subsequently dried under a laminar flow. Electron micrographs were obtained using a 120 KeV Tecnai TEM (FEI) with a BMEagel detector recorded

at a nominal 49,000 x magnification with calibrated pixel sizes of 4.37 Å pixel⁻¹.

Initial structural analysis of αB -AXA fibrils was performed on EM images of negatively stained specimens. Preliminary fibrillar crossover dimensions were obtained by direct measurements using the Fiji software 80 . For initial 2D and 3D analysis, individual filament segments were selected using the 'helixboxer' tool in EMAN2 and extracted using a box size of 88 pixels and a 90% box overlap. Extracted particles were imported into Relion for class averaging and a de novo initial model was generated in EMAN2.

For cage-like assemblies of αB -AXA, particles were automatically picked using the threshold picking tool in EMAN2 and extracted using a box size of 84 or 112 pixels before being imported into Relion for 2D class averaging. Single particle distribution analysis was performed in Fiji⁸⁰, using established methods¹⁶. Briefly, an FFT bandpass filter was applied to each image stack using the filter settings in FIJI (filter large structures at 60 pixels, filter small structures at 4 pixels). Next, the maximum filter was used with a default radius of 2 pixels followed by background subtraction (rolling ball radius of 20 pixels) was used on each micrograph stack. The filtered and background subtracted micrographs were subsequently binarized (with dark background). Background noise removal with the Remove Outliers tool and erosion/dilation of binarized segments were tuned to optimize segmentation results. The FIJI Analyze Particles tool was used to collect Feret diameter measurements.

Cryo-Electron Microscopy

αB-AXA samples that had undergone elongation at room temperature for about four weeks were prepared for cryo-EM analysis. Elongated samples were dialyzed with a 1 MDa m.w.c.o. membrane, to remove any residual globular assemblies. For cryo-grid preparation, 3 μL drops of the sample were applied to R2/1 Quantifoil grids at a concentration of 0.5 mg/mL and plunge frozen using a Vitrobot Mk III autoplunger (FEI). Image acquisition was conducted on a Titan Krios G3 (Thermo-Fisher), equipped with a K3 direct electron detector (Gatan). The completed dataset was obtained using automated data collection routines with SerialEM83, resulting in 10,654 micrographs with a defocus range of 0.5 to 2 μm. Movies were recorded with a physical pixel size of 0.788 Å/pixel (0.394 Å/pixel super-resolution) and a total electron dose of 50 e⁻/pixel.

For image processing, electron micrographs were imported into cryoSPARC⁴⁶ in two subsets (containing 4585 and 6069 micrographs), where they were motion corrected and CTF fit. The Filament Tracer module in cryoSPARC was used to pick particles from a random subset of 10 micrographs with fibril diameter 160 Å and a segment overlap of 0.2 x diameter, which were then averaged using 2D classification to generate initial templates for subsequent particle picking. This was then applied to an extended subset of 100 micrographs, leading to a total of 27,990 segments. These segments were then classified to generate a refined template and applied to the entire dataset, yielding 2.2 million segments with a box size of 400 pixels.

Several rounds of 2D classification were applied to the full dataset with a box size of 400 pixels to first remove non-protein and low-quality segments. Later classification steps sought to remove segments with poor alignment near the edge of the box. A total of 1,406,353 well-aligned segments were then extracted using a box size of 288 pixels to generate an initial model from *ab initio refinement* with a total of 4 classes. The highest quality class had initial helical parameters of 31° twist and 39 Å rise. These parameters were iteratively improved through multiple rounds of helical refinement with D2 symmetry, resulting in the final helical parameters of 31.7° twist and a rise of 40.6 Å at a resolution of 3.54 Å. This particle stack was then masked to isolate the internal D2 symmetric unit and subjected to local refinement with unchanged box size, reaching a resolution of 3.41 Å. The refined particle stack was then signal subtracted before applying 3D

classification in cryoSPARC with 4 classes. The highest quality class contained 370,722 particles. This particle set was then locally refined with D2 symmetry to reach a final resolution of 3.36 Å (gold-standard FSC; see Supplemental Table 1 and Supplemental Fig. 3). Additional workflows were extensively assayed incorporating 3D classification and local refinement in cryoSPARC (as well as in Relion⁸⁴), but these did not lead to appreciable improvement of resolved features.

Model building

Atomic models for the asymmetric unit were built starting with the previously reported crystal structure of the human αB-crystallin ACD dimer (PDB 2WJ7)²⁷, which was fitted into the unsharpened cryo-EM map obtained from local refinement. The model of the ACD dimer was first rigidly fit into the map with ChimeraX⁸⁵ and then flexibly fit using ISOLDE⁸⁶. The CT-loop at the inner seam and CT-IXI motifs at both the inner- and outer-seam were sufficiently resolved to be manually built in COOT directly from the local refinement map. The CT-loop along the outer seam though was lost in the local refinement job. Model building in this region required modeling of several asymmetric units in a lower resolution map containing multiple helical rungs and the connecting loops were built in COOT and fit flexibly with ISOLDE. A final model was then obtained through iterations of refinement in Phenix87 and adjustments in both ISOLDE and COOT88 until refinement statistics converged, as judged by Molprobity⁸⁹ (see Supplemental Table 1 and Supplemental Fig. 4).

2D and 3D variability analysis

Conformational variability of fibrils observed in 2D classification results obtained from cryoSPARC was assessed by hand in Fiji⁸⁰. A total of eight representative classes were chosen based on presence of bend angle (n=4) or crossover distance (n=4), as examples of the variability observed from the 2D classification results. Crossover distances in 2D classes was determined by measuring distance between successive cross-over points observed in projection, defined as either the neighboring narrowest or broadest regions of the fibril. Bend angles were measured using the angle measurement tool in Fiji, covering the three crossovers that were visible in a single 2D class.

To further assess the intrinsic variability of the helical assembly, 3D variability analysis (3DVA) was conducted using cryoSPARC⁶¹. Initially, particles were extracted with a box size of 800 pixels to capture the variance along the length of the fibril. This analysis revealed distinct principal components describing both stretching and bending modes of variance. To enhance the quality of the volume series for the bending mode, the "intermediates output type" was used, which reconstructs the volume for every individual frame rather than interpolating from a central point. This method yielded a more well-defined volume series (Supplemental Movie 2).

The fibril's stretching mode was less obvious in this initial analysis. To enhance this feature, particles were culled from the 2D classification process to remove classes that exhibited bent conformations and performed 3DVA on the resultant particle stack. This approach revealed distinct principal components describing the stretching mode with increased magnitude over the previous approach. However, in this case, the density of the volume series remained poor near the edges of the box. To address this issue, particles from either end of the volume series were selected and used to reconstruct the endpoints of the component. The resulting linear interpolation between the two volumes resulted in a higher quality volume series (Supplemental Movie 2).

Chaperone assays

Chaperone assays were carried out by monitoring the suppression of light scattering caused by chemically induced aggregation of the model client, lysozyme (Sigma, mass-spec grade). For all assays, lysozyme was prepared at a final concentration of $10\,\mu M$ in a

reaction buffer of 20 mM HEPES, 100 mM NaCl and 1 mM EDTA (pH 7.4). TCEP was added to a final concentration of 1 mM to induce the aggregation of lysozyme, which was tracked by an increase of turbidity at 360 nm (Tecan Infinite 200 Pro). All assays included reactions containing lysozyme only (negative control) and αB -wt (positive control).

For assays conducted on αB -AXA in the native-like morphology, samples were fully converted to the globular state by incubating at 42° C for ~18 hours. Full conversion of these samples was confirmed by DLS and EM. Chaperone assays were conducted at 37° C and light scattering was monitored for 4 hours, at which point the reactions had reached steady-state. αB -AXA assemblies were assayed against $10~\mu M$ lysozyme over a range of concentrations ($10~-40~\mu M$). Assays conducted using αB -wt were performed under these same conditions. Chaperone activity was calculated from the turbidity traces and converted to percent protection versus lysozyme-only conditions.

For assays conducted on αB -AXA fibrils, protein stocks of 3 mg/mL were elongated at 25° C and dialyzed overnight in reaction buffer using a 1MDa m.w.c.o. membrane to remove residual native-like assemblies (as confirmed by EM). Chaperone assays for these samples were conducted at 25° C to maintain stability of the fibril assembly. Light scattering was monitored for 18 hours to account for slower aggregation kinetics of lysozyme at these reduced temperatures. αB -AXA fibrils were assayed against $10\,\mu M$ lysozyme over a range of concentrations (1–100 μM). EM grids were prepared on negatively stained samples of the end-point reactions and imaged as described above.

Statistical analysis

Raw turbidity data from chaperone assays were processed by first min-max normalizing. Percent protection was determined by the percent reduction in turbidity compared to the lysozyme-only control samples. All chaperone assays were performed in replicate (n = 6-9). However, due to sample limitations some measurements were limited to only one biological replicate with multiple technical replicates. Statistics were therefore calculated using the combination of biological and technical replicates from each experimental condition (detailed in the figure legends) using two-tailed t-test. Cryo-EM and NS-EM sample sizes were not predetermined. A cryo-EM dataset of 1,406,353 particles was collected from a total of 10,654 micrographs. The size of this dataset was estimated based on instrument availability and expected target resolution. Single particle image data was excluded based on the absence of high-resolution features (e.g., secondary structural elements). Cryo-EM data processing was replicated by using alternative image processing software (cryoSPARC and RELION), yielding similar results. Cryo-EM data collection was replicated on 2 independent samples that were eventually merged for data processing. Single particle image data was split randomly into two groups and processed in the same way to calculate Fourier-shell correlation coefficients, in accordance to Gold-Standard methods. Samples were not further allocated into groups, outside of what is performed by the computational image analysis programs used in this work. Investigators were not blinded during data acquisition or analysis. Blinded studies in this case were not possible because the investigator performing the experiments and analysis also contributed to isolation of the specimen being analyzed.

Figure preparation

Structural models and cryo-EM density maps were visualized and prepared for presentation using ChimeraX⁸⁵. Cartoon illustrations were inspired by previous work by Reinle et al³., and prepared in PowerPoint. Final figures were composed in Photoshop.

Al-assisted technologies

During the preparation of this work the authors used ChatGPT to help revise portions of the text to improve readability. After using this tool, the authors reviewed and edited the content as needed and take full responsibility for the content of the publication.

Reporting summary

Further information on research design is available in the Nature Portfolio Reporting Summary linked to this article.

Data availability

Cryo-EM density maps have been deposited to the Electron Microscopy Data Bank (EMD-44477 [https://www.ebi.ac.uk/pdbe/entry/emdb/EMD-44477]). Coordinates for atomic models have been deposited to the Protein Data Bank (PDB: 9BEE). The original multiframe micrographs have been deposited to Electron Microscopy Public Image Archive (EMPIAR-12449 [https://www.ebi.ac.uk/empiar/EMPIAR-12449]). Negative stain EM datasets and uncropped micrographs have been deposited to zenodo [https://doi.org/10.5281/zenodo.14113490]. Source data are provided with this paper. Plasmids used for protein expression are available upon request. Previously published models used for comparative analysis and initial modeling can be found here: (PDB: 2WJ7) and (2NOK [https://www.rcsb.org/structure/2NOK]). Source data are provided with this paper.

References

- Horwitz, J. Alpha-crystallin can function as a molecular chaperone. Proc. Natl Acad. Sci. USA 89, 10449–10453 (1992).
- Jakob, U., Gaestel, M., Engel, K. & Buchner, J. Small heat shock proteins are molecular chaperones. J. Biol. Chem. 268, 1517–1520 (1993).
- Reinle, K., Mogk, A. & Bukau, B. The diverse functions of small heat shock proteins in the proteostasis network. J. Mol. Biol. 434, 167157 (2022).
- Mogk, A., Bukau, B. & Kampinga, H. H. Cellular handling of protein aggregates by disaggregation machines. *Mol. Cell* 69, 214–226 (2018).
- 5. Kappe, G. et al. The human genome encodes 10 alpha-crystallin-related small heat shock proteins: HspB1-10. *Cell Stress Chaperones* **8**, 53–61 (2003).
- de Jong, W. W., Caspers, G. J. & Leunissen, J. A. Genealogy of the alpha-crystallin-small heat-shock protein superfamily. *Int J. Biol. Macromol.* 22, 151–162 (1998).
- 7. Iwaki, T., Kume-Iwaki, A. & Goldman, J. E. Cellular distribution of alpha B-crystallin in non-lenticular tissues. *J. Histochem Cytochem* **38**, 31–39 (1990).
- Slingsby, C. & Wistow, G. J. Functions of crystallins in and out of lens: roles in elongated and post-mitotic cells. *Prog. Biophys. Mol. Biol.* 115, 52–67 (2014).
- Bakthisaran, R., Tangirala, R. & Rao, Ch. M. Small heat shock proteins: role in cellular functions and pathology. *Biochim Biophys.* Acta 1854, 291–319 (2015).
- Sarparanta, J., Jonson, P. H., Kawan, S. & Udd, B. Neuromuscular diseases due to chaperone mutations: a review and some new results. *Int. J. Mol. Sci.* 21, 1409 (2020).
- Horwitz, J. Alpha crystallin: the quest for a homogeneous quaternary structure. Exp. Eye Res 88, 190–194 (2009).
- 12. Haslbeck, M., Weinkauf, S. & Buchner, J. Small heat shock proteins: simplicity meets complexity. *J. Biol. Chem.* **294**, 2121–2132 (2019).
- Haley, D. A., Horwitz, J. & Stewart, P. L. The small heat-shock protein, alphaB-crystallin, has a variable quaternary structure. J. Mol. Biol. 277, 27–35 (1998).
- Aquilina, J. A., Benesch, J. L., Bateman, O. A., Slingsby, C. & Robinson, C. V. Polydispersity of a mammalian chaperone: mass

- spectrometry reveals the population of oligomers in alphaB-crystallin. *Proc. Natl Acad. Sci. USA* **100**. 10611–10616 (2003).
- Inoue, R. et al. New insight into the dynamical system of alphaBcrystallin oligomers. Sci. Rep. 6, 29208 (2016).
- Miller, A. P., O'Neill, S. E., Lampi, K. J. & Reichow, S. L. The alphacrystallin chaperones undergo a Quasi-ordered Co-aggregation process in response to saturating client interaction. *J. Mol. Biol.*436, 168499 (2024).
- van den Oetelaar, P. J., van Someren, P. F., Thomson, J. A., Siezen, R. J. & Hoenders, H. J. A dynamic quaternary structure of bovine alpha-crystallin as indicated from intermolecular exchange of subunits. *Biochemistry* 29, 3488–3493 (1990).
- Bova, M. P., McHaourab, H. S., Han, Y. & Fung, B. K. Subunit exchange of small heat shock proteins. analysis of oligomer formation of alphaA-crystallin and Hsp27 by fluorescence resonance energy transfer and site-directed truncations. J. Biol. Chem. 275, 1035–1042 (2000).
- Baldwin, A. J. et al. Quaternary dynamics of alphaB-crystallin as a direct consequence of localised tertiary fluctuations in the C-terminus. J. Mol. Biol. 413, 310–320 (2011).
- 20. Inoue, R. et al. Elucidation of the mechanism of subunit exchange in alphaB crystallin oligomers. *Sci. Rep.* **11**, 2555 (2021).
- Peschek, J. et al. Regulated structural transitions unleash the chaperone activity of alphaB-crystallin. Proc. Natl Acad. Sci. USA 110, E3780–E3789 (2013).
- de Jong, W. W., Leunissen, J. A. & Voorter, C. E. Evolution of the alpha-crystallin/small heat-shock protein family. *Mol. Biol. Evol.* 10, 103–126 (1993).
- Kriehuber, T. et al. Independent evolution of the core domain and its flanking sequences in small heat shock proteins. FASEB J. 24, 3633–3642 (2010).
- Jehle, S. et al. N-terminal domain of alphaB-crystallin provides a conformational switch for multimerization and structural heterogeneity. Proc. Natl Acad. Sci. USA 108, 6409–6414 (2011).
- Carver, J. A., Aquilina, J. A., Truscott, R. J. & Ralston, G. B. Identification by 1H NMR spectroscopy of flexible C-terminal extensions in bovine lens alpha-crystallin. FEBS Lett. 311, 143–149 (1992).
- Shi, J., Koteiche, H. A., McHaourab, H. S. & Stewart, P. L. Cryoelectron microscopy and EPR analysis of engineered symmetric and polydisperse Hsp16.5 assemblies reveals determinants of polydispersity and substrate binding. *J. Biol. Chem.* 281, 40420–40428 (2006).
- Bagneris, C. et al. Crystal structures of alpha-crystallin domain dimers of alphaB-crystallin and Hsp2O. J. Mol. Biol. 392, 1242–1252 (2009).
- Laganowsky, A. et al. Crystal structures of truncated alphaA and alphaB crystallins reveal structural mechanisms of polydispersity important for eye lens function. *Protein Sci.* 19, 1031–1043 (2010).
- Clark, A. R., Naylor, C. E., Bagneris, C., Keep, N. H. & Slingsby, C. Crystal structure of R120G disease mutant of human alphaBcrystallin domain dimer shows closure of a groove. *J. Mol. Biol.* 408, 118–134 (2011).
- Hochberg, G. K. et al. The structured core domain of alphaBcrystallin can prevent amyloid fibrillation and associated toxicity. Proc. Natl Acad. Sci. USA 111, E1562–E1570 (2014).
- Rajagopal, P. et al. A conserved histidine modulates
 HSPB5 structure to trigger chaperone activity in response to stressrelated acidosis. Elife 4, e07304 (2015).
- Treweek, T. M., Rekas, A., Walker, M. J. & Carver, J. A. A quantitative NMR spectroscopic examination of the flexibility of the C-terminal extensions of the molecular chaperones, alphaA- and alphaBcrystallin. Exp. Eye Res 91, 691–699 (2010).
- Pasta, S. Y., Raman, B., Ramakrishna, T. & Rao, Ch,M. The IXI/V motif in the C-terminal extension of alpha-crystallins: alternative interactions and oligomeric assemblies. *Mol. Vis.* 10, 655–662 (2004).

- Delbecq, S. P., Jehle, S. & Klevit, R. Binding determinants of the small heat shock protein, alphaB-crystallin: recognition of the 'IxI' motif. EMBO J. 31, 4587–4594 (2012).
- Ghosh, J. G. & Clark, J. I. Insights into the domains required for dimerization and assembly of human alphaB crystallin. *Protein Sci.* 14, 684–695 (2005).
- 36. Clouser, A. F. et al. Interplay of disordered and ordered regions of a human small heat shock protein yields an ensemble of 'quasi-ordered' states. *Elife* **8**, e50259 (2019).
- Ghosh, J. G., Shenoy, A. K. Jr. & Clark, J. I. N- and C-Terminal motifs in human alphaB crystallin play an important role in the recognition, selection, and solubilization of substrates. *Biochemistry* 45, 13847–13854 (2006).
- 38. Mainz, A. et al. The chaperone alphaB-crystallin uses different interfaces to capture an amorphous and an amyloid client. *Nat. Struct. Mol. Biol.* **22**, 898–905 (2015).
- 39. Jehle, S. et al. Solid-state NMR and SAXS studies provide a structural basis for the activation of alphaB-crystallin oligomers. *Nat. Struct. Mol. Biol.* **17**, 1037–1042 (2010).
- Peschek, J. et al. The eye lens chaperone alpha-crystallin forms defined globular assemblies. *Proc. Natl Acad. Sci. USA* 106, 13272–13277 (2009).
- 41. Braun, N. et al. Multiple molecular architectures of the eye lens chaperone alphaB-crystallin elucidated by a triple hybrid approach. *Proc. Natl Acad. Sci. USA* **108**, 20491–20496 (2011).
- 42. Kaiser, C. J. O. et al. The structure and oxidation of the eye lens chaperone alphaA-crystallin. *Nat. Struct. Mol. Biol.* **26**, 1141–1150 (2019).
- 43. Siezen, R. J., Bindels, J. G. & Hoenders, H. J. The quaternary structure of bovine alpha-crystallin. Effects of variation in alkaline pH, ionic strength, temperature and calcium ion concentration. *Eur. J. Biochem* 111, 435–444 (1980).
- Siezen, R. J., Bindels, J. G. & Hoenders, H. J. The quaternary structure of bovine alpha-crystallin. Size and charge microheterogeneity: more than 1000 different hybrids? *Eur. J. Biochem* 91, 387–396 (1978).
- Selivanova, O. M. & Galzitskaya, O. V. Structural and functional peculiarities of alpha-crystallin. *Biology (Basel)* 9, 85 (2020).
- Punjani, A., Rubinstein, J. L., Fleet, D. J. & Brubaker, M. A. cryoS-PARC: algorithms for rapid unsupervised cryo-EM structure determination. *Nat. Methods* 14, 290–296 (2017).
- Vicart, P. et al. A missense mutation in the alphaB-crystallin chaperone gene causes a desmin-related myopathy. *Nat. Genet* 20, 92–95 (1998).
- 48. Litt, M. et al. Autosomal dominant congenital cataract associated with a missense mutation in the human alpha crystallin gene CRYAA. *Hum. Mol. Genet* **7**, 471–474 (1998).
- 49. Fichna, J. P. et al. A novel dominant D109A CRYAB mutation in a family with myofibrillar myopathy affects alphaB-crystallin structure. *BBA Clin.* **7**, 1–7 (2017).
- Sacconi, S. et al. A novel CRYAB mutation resulting in multisystemic disease. Neuromuscul. Disord. 22, 66–72 (2012).
- Bova, M. P. et al. Mutation R120G in alphaB-crystallin, which is linked to a desmin-related myopathy, results in an irregular structure and defective chaperone-like function. *Proc. Natl Acad. Sci. USA* **96**, 6137–6142 (1999).
- 52. Treweek, T. M. et al. R120G alphaB-crystallin promotes the unfolding of reduced alpha-lactalbumin and is inherently unstable. *FEBS J.* **272**, 711–724 (2005).
- Hafizi, M. et al. Structural and functional studies of D109A human alphaB-crystallin contributing to the development of cataract and cardiomyopathy diseases. *PLoS One* 16, e0260306 (2021).
- Ghahramani, M. et al. Structural and functional characterization of D109H and R69C mutant versions of human alphaB-crystallin: The

- biochemical pathomechanism underlying cataract and myopathy development. *Int J. Biol. Macromol.* **146**. 1142–1160 (2020).
- 55. Kim, K. K., Kim, R. & Kim, S. H. Crystal structure of a small heat-shock protein. *Nature* **394**, 595–599 (1998).
- Haley, D. A., Bova, M. P., Huang, Q. L., McHaourab, H. S. & Stewart,
 P. L. Small heat-shock protein structures reveal a continuum from symmetric to variable assemblies. J. Mol. Biol. 298, 261–272 (2000).
- 57. White, H. E. et al. Multiple distinct assemblies reveal conformational flexibility in the small heat shock protein Hsp26. *Structure* **14**, 1197–1204 (2006).
- Shi, J. et al. Cryoelectron microscopy analysis of small heat shock protein 16.5 (Hsp16.5) complexes with T4 lysozyme reveals the structural basis of multimode binding. J. Biol. Chem. 288, 4819–4830 (2013).
- Sluchanko, N. N. et al. Structural basis for the interaction of a human small heat shock protein with the 14-3-3 universal signaling regulator. Structure 25, 305–316 (2017).
- Woods, C. N., Ulmer, L. D., Guttman, M., Bush, M. F. & Klevit, R. E. Disordered region encodes alpha-crystallin chaperone activity toward lens client gammaD-crystallin. *Proc. Natl Acad. Sci. USA* 120, e2213765120 (2023).
- 61. Punjani, A. & Fleet, D. J. 3D variability analysis: resolving continuous flexibility and discrete heterogeneity from single particle cryo-EM. *J. Struct. Biol.* **213**, 107702 (2021).
- 62. Shi, X. et al. Small heat shock protein AgsA forms dynamic fibrils. *FEBS Lett.* **585**, 3396–3402 (2011).
- 63. Al-Ansari, M. et al. The major inducible small heat shock protein HSP20-3 in the tardigrade Ramazzottius varieornatus forms filament-like structures and is an active chaperone. *Cell Stress Chaperones* **29**, 51–65 (2024).
- van Montfort, R. L., Basha, E., Friedrich, K. L., Slingsby, C. & Vierling,
 E. Crystal structure and assembly of a eukaryotic small heat shock protein. *Nat. Struct. Biol.* 8, 1025–1030 (2001).
- Fleckenstein, T. et al. The chaperone activity of the developmental small heat shock protein Sip1 is regulated by pH-dependent conformational changes. Mol. Cell 58, 1067–1078 (2015).
- Clark, A. R. et al. Terminal regions confer plasticity to the tetrameric assembly of human HspB2 and HspB3. J. Mol. Biol. 430, 3297–3310 (2018).
- 67. Klevit, R. E. Peeking from behind the veil of enigma: emerging insights on small heat shock protein structure and function. *Cell Stress Chaperones* **25**, 573–580 (2020).
- Ghosh, J. G., Estrada, M. R. & Clark, J. I. Interactive domains for chaperone activity in the small heat shock protein, human alphaB crystallin. *Biochemistry* 44, 14854–14869 (2005).
- Bhattacharyya, J., Padmanabha Udupa, E. G., Wang, J. & Sharma, K. K. Mini-alphaB-crystallin: a functional element of alphaB-crystallin with chaperone-like activity. *Biochemistry* 45, 3069–3076 (2006).
- Pasta, S. Y., Raman, B., Ramakrishna, T. & Rao, Ch,M. Role of the conserved SRLFDQFFG region of alpha-crystallin, a small heat shock protein. Effect on oligomeric size, subunit exchange, and chaperone-like activity. J. Biol. Chem. 278, 51159–51166 (2003).
- Muhlhofer, M. et al. Phosphorylation activates the yeast small heat shock protein Hsp26 by weakening domain contacts in the oligomer ensemble. *Nat. Commun.* 12, 6697 (2021).
- Biswas, S., Garg, P., Dutta, S. & Suguna, K. Multiple nanocages of a cyanophage small heat shock protein with icosahedral and octahedral symmetries. Sci. Rep. 11, 21023 (2021).
- Datta, S. A. & Rao, C. M. Differential temperature-dependent chaperone-like activity of alphaA- and alphaB-crystallin homoaggregates. J. Biol. Chem. 274, 34773–34778 (1999).
- Reddy, G. B., Das, K. P., Petrash, J. M. & Surewicz, W. K. Temperature-dependent chaperone activity and structural

- properties of human alphaA- and alphaB-crystallins. *J. Biol. Chem.* **275**, 4565–4570 (2000).
- 75. Aquilina, J. A. et al. Subunit exchange of polydisperse proteins: mass spectrometry reveals consequences of alphaA-crystallin truncation. *J. Biol. Chem.* **280**, 14485–14491 (2005).
- 76. Siezen, R. J., Bindels, J. G. & Hoenders, H. J. The interrelationship between monomeric, oligomeric and polymeric alpha-crystallin in the calf lens nucleus. *Exp. Eye Res* **28**, 551–567 (1979).
- Strauch, A. et al. The permanently chaperone-active small heat shock protein Hsp17 from Caenorhabditis elegans exhibits topological separation of its N-terminal regions. J. Biol. Chem. 299, 102753 (2023).
- Stromer, T., Ehrnsperger, M., Gaestel, M. & Buchner, J. Analysis of the interaction of small heat shock proteins with unfolding proteins. J. Biol. Chem. 278, 18015–18021 (2003).
- 79. Aquilina, J. A. & Watt, S. J. The N-terminal domain of alphaB-crystallin is protected from proteolysis by bound substrate. *Biochem Biophys. Res Commun.* **353**, 1115–1120 (2007).
- 80. Schindelin, J. et al. Fiji: an open-source platform for biologicalimage analysis. *Nat. Methods* **9**, 676–682 (2012).
- 81. Tang, G. et al. EMAN2: an extensible image processing suite for electron microscopy. *J. Struct. Biol.* **157**, 38–46 (2007).
- 82. Scheres, S. H. RELION: implementation of a Bayesian approach to cryo-EM structure determination. *J. Struct. Biol.* **180**, 519–530 (2012).
- 83. Mastronarde, D. N. Automated electron microscope tomography using robust prediction of specimen movements. *J. Struct. Biol.* **152**, 36–51 (2005).
- 84. He, S. & Scheres, S. H. W. Helical reconstruction in RELION. *J. Struct. Biol.* **198**, 163–176 (2017).
- 85. Goddard, T. D. et al. UCSF ChimeraX: meeting modern challenges in visualization and analysis. *Protein Sci.* 27, 14–25 (2018).
- 86. Croll, T. I. ISOLDE: a physically realistic environment for model building into low-resolution electron-density maps. *Acta Crystallogr D. Struct. Biol.* **74.** 519–530 (2018).
- 87. Afonine, P. V. et al. Real-space refinement in PHENIX for cryo-EM and crystallography. *Acta Crystallogr D. Struct. Biol.* **74**, 531–544 (2018).
- 88. Emsley, P. & Cowtan, K. Coot: model-building tools for molecular graphics. *Acta Crystallogr. D.* **60**, 2126–2132 (2004).
- Williams, C. J. et al. MolProbity: More and better reference data for improved all-atom structure validation. *Protein Sci.* 27, 293–315 (2018).

Acknowledgements

We thank Dr. Kirsten Lampi for helpful discussions. We are grateful for instrumentation access and training provided by the staff at the OHSU Multiscale Microscopy Core and Advanced Computing center, and the Pacific Northwest Center for CryoEM (supported by NIH Grant R24GM154185) with the assistance of Dr. Janette Myers. The research was funded by NIH grants R01EY030987 and R35GM124779 (to S.L.R.) and fellowships F31EY033230 (to R.M.) and F31EY033226 (to A.P.M.).

Author contributions

R.M. performed cryo-EM and functional experiments and analyzed these data; R.N. and A.P.M. contributed to collection of NS-EM data and structural analyzes; S.L.R. and R.M. conceived of the study and prepared the initial manuscript. All authors contributed to the final revision of the manuscript.

Competing interests

Authors declare no competing interests.

Additional information

Supplementary information The online version contains supplementary material available at https://doi.org/10.1038/s41467-024-54647-7.

Correspondence and requests for materials should be addressed to Steve L. Reichow.

Peer review information *Nature Communications* thanks the anonymous reviewers for their contribution to the peer review of this work. A peer review file is available.

Reprints and permissions information is available at http://www.nature.com/reprints

Publisher's note Springer Nature remains neutral with regard to jurisdictional claims in published maps and institutional affiliations.

Open Access This article is licensed under a Creative Commons Attribution-NonCommercial-NoDerivatives 4.0 International License, which permits any non-commercial use, sharing, distribution and reproduction in any medium or format, as long as you give appropriate credit to the original author(s) and the source, provide a link to the Creative Commons licence, and indicate if you modified the licensed material. You do not have permission under this licence to share adapted material derived from this article or parts of it. The images or other third party material in this article are included in the article's Creative Commons licence, unless indicated otherwise in a credit line to the material. If material is not included in the article's Creative Commons licence and your intended use is not permitted by statutory regulation or exceeds the permitted use, you will need to obtain permission directly from the copyright holder. To view a copy of this licence, visit http://creativecommons.org/licenses/by-nc-nd/4.0/.

© The Author(s) 2024